

# HYDRODYNAMICS OF TURBID UNDERFLOWS. I: FORMULATION AND NUMERICAL ANALYSIS

By Scott F. Bradford<sup>1</sup> and Nikolaos D. Katopodes,<sup>2</sup> Members, ASCE

**ABSTRACT:** A mathematical model is developed for unsteady, two-dimensional, single-layer, depth-averaged turbid underflows driven by nonuniform, noncohesive sediment. The numerical solution is obtained by a high-resolution, total variation diminishing, finite-volume numerical model, which is known to capture sharp fronts accurately. The monotone upstream scheme for conservation laws is used in conjunction with predictor-corrector time-stepping to provide a second-order accurate solution. Flux-limiting is implemented to prevent the development of spurious oscillations near discontinuities. The model also possesses the capability to track the evolution and development of an erodible bed, due to sediment entrainment and deposition. This is accomplished by solving a bed-sediment conservation equation at each time step, independent of the hydrodynamic equations, with a predictor-corrector method. The model is verified by comparison to experimental data for currents driven by uniform and nonuniform sediment.

## INTRODUCTION

There is great interest in turbidity currents because of their profound impact on the morphology of the continental shelves and ocean basins of the world. Turbidity currents are credited with delivering the majority of sediment to the deep sea where a submarine fan typically forms (Stow et al. 1985). Turbidity currents can also be highly erosive and therefore are believed to have carved out many of the submarine canyons found on the continental shelf (Parker 1982). In addition, many submarine fans constitute major hydrocarbon reservoirs around the world (Wilde et al. 1985), and therefore a clear and complete knowledge of submarine fan morphology is crucial for effectively exploring and exploiting these reservoirs.

An additional concern is the destructive effect that turbidity currents have on underwater structures, such as cables, pipelines, foundations, and moorings. One of the first documented examples of the destructive power of turbidity currents was the breaking of deep sea telegraph cables following the 1929 Grand Banks earthquake (Heezen and Ewing 1952). Dengler and Wilde (1987) utilized a numerical model for design purposes to simulate turbidity currents and estimate the resulting forces exerted on underwater pipelines.

Laboratory experiments have frequently been performed to study turbidity currents, but the results are only roughly applicable to large-scale geophysical events. Middleton (1966) recommended Froude number scaling to capture the hydraulics of the flow. This, however, precludes the possibility of obtaining Reynolds number similarity. Consequently, laboratory models will always over-emphasize viscous effects. The Coriolis acceleration, surface tension, and sediment phase would likewise be scaled incorrectly.

Field observations of turbidity currents are rare because of the unpredictability and destructive nature of the events. The velocity estimates of the event that occurred after the 1929 Grand Banks earthquake came from the time between cable breaks on the Atlantic floor (Heezen and Ewing 1952), while in situ measuring equipment is often lost or destroyed prior to the completion of the event (Inman et al. 1976). However,

flows have been observed at the mouths of rivers and at mining locations (Hay 1987; Normark 1989), which, because of their large scale, are probably more representative of geophysical events than are laboratory models.

In addition to field observations, there have been many attempts at reconstructing turbidity currents from the depositional record, i.e., deposited surface sediments, core samples, and channel morphology (Komar 1977; Reynolds 1987). However, bottom morphology has been measured primarily through the use of sonar scans. The great depth at which many submarine fans and channels are located introduces uncertainty into these results and renders their acquisition both dangerous and expensive (Flood and Damuth 1987). Also, the use of surface sediment grain size alone may yield drastic underestimates of the flow velocity (Hiscott 1984).

Due to the aforementioned problems with experimental and observational investigations, theoretical models would seem to be an attractive alternative for studying turbidity currents. A comprehensive review of theoretical models has been performed by Bradford (1996). Recently, theoretical modeling has received greater attention because of the increased computational power and improved numerical methods available. Numerical simulations allow for a greater understanding of turbidity currents and their depositional mechanics by examining the interdependence between flow and sedimentation parameters in a detailed manner, without the scaling limitations of experiments and the unpredictability and expense of field observations. Imran et al. (1998) used a finite-difference scheme to predict channel inception by assuming an antecedent turbid flow thickness to be present in the solution domain. In this paper, the most recent closure relations have been coupled with advanced numerical techniques to produce a turbidity current model that has the ability not only to predict the flow hydrodynamics, but also to simulate the resulting sedimentation and bed evolution. This then allows for the study of the complex interaction between the flow and its environment, something not possible by simpler models.

## GOVERNING EQUATIONS

The equations that form the basis of the model are the vertically integrated, fluid, momentum, and sediment conservation equations. These equations form a coupled system of nonlinear, hyperbolic, partial differential equations. Turbidity currents occur as underflows in the deep sea, and when the flow thickness does not exceed approximately 7.5% of the overall ambient fluid depth, the hydrodynamics of the turbidity current can be accurately described by a "single-layer" formulation (Huppert and Simpson 1980). A sketch of a turbid underflow is presented in Fig. 1. These equations are valid for the flow

<sup>1</sup>Mech. Engr., Naval Research Laboratory, Washington, DC 20375.

<sup>2</sup>Prof., Dept. of Civ. and Envir. Engrg., Univ. of Michigan, Ann Arbor, MI 48109.

Note. Discussion open until March 1, 2000. Separate discussions should be submitted for the individual papers in this symposium. To extend the closing date one month, a written request must be filed with the ASCE Manager of Journals. The manuscript for this paper was submitted for review and possible publication on May 19, 1997. This paper is part of the *Journal of Hydraulic Engineering*, Vol. 125, No. 10, October, 1999. ©ASCE, ISSN 0733-9429/99/0010-1006-1015/\$8.00 + \$.50 per page. Paper No. 15826.

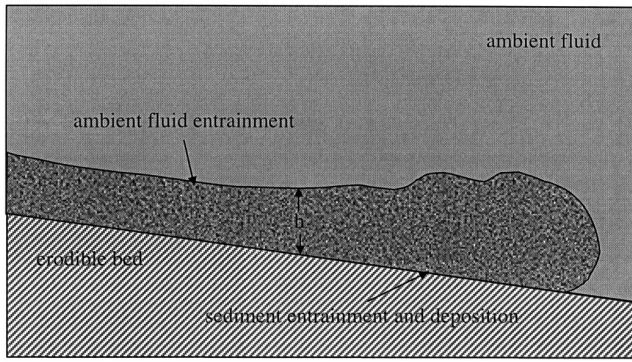


FIG. 1. Sketch of Turbid Underflow

of a 2D turbidity current driven by a nonuniform, noncohesive sediment, which is flowing beneath an infinitely deep layer of constant density, quiescent fluid, and are written in integral form as (Parker et al. 1986)

$$\frac{\partial}{\partial t} \int_{\Omega} \mathbf{U} d\Omega + \oint_{\partial\Omega} (\mathbf{F} dy - \mathbf{G} dx) = \int_{\Omega} \mathbf{Q} d\Omega \quad (1)$$

where  $\mathbf{U}^T = (h, hU, hV, hC_1, \dots, hC_{n_s})$  is the vector of conservative variables, and

$$\mathbf{F} = \begin{pmatrix} hU \\ hU^2 + \frac{1}{2} gh^2 RC_T \\ hUV \\ hUC_1 \\ \vdots \\ hUC_{n_s} \end{pmatrix} \quad (2)$$

$$\mathbf{G} = \begin{pmatrix} hV \\ hUV \\ hV^2 + \frac{1}{2} gh^2 RC_T \\ hVC_1 \\ \vdots \\ hVC_{n_s} \end{pmatrix} \quad (3)$$

$$\mathbf{Q} = \begin{pmatrix} E_w \sqrt{U^2 + V^2} \\ -ghRC_T s_x - u_*^2 \\ -ghRC_T s_y - v_*^2 \\ v_{s_1}(p_1 E_{s_1} - c_{b_1}) \\ \vdots \\ v_{s_{n_s}}(p_{n_s} E_{s_{n_s}} - c_{b_{n_s}}) \end{pmatrix} \quad (4)$$

where

$$RC_T = \sum_{i=1}^{n_s} R_i C_i \quad (5)$$

The term  $h$  represents the flow thickness;  $U$  and  $V$  = vertically averaged velocities in the  $x$  and  $y$  directions, respectively; and  $C_i$  = vertically averaged volume concentration of the  $i$ th sediment. The total number of sediments contained in the current is denoted by  $n_s$ . The parameter  $R_i = (\rho_{s_i} - \rho)/\rho$ , where  $\rho_{s_i}$  is the density of the  $i$ th sediment and  $\rho$  is the density of the ambient water, while  $g$  denotes the acceleration due to gravity.

The term  $E_w$  is a fluid entrainment coefficient. The following expression (Parker et al. 1987) is used in the present model:

$$E_w = \frac{0.075}{\sqrt{1 + 718 \text{Ri}^{2.4}}} \quad (6)$$

where  $\text{Ri}$  = Richardson number and is defined as

$$\text{Ri} = \frac{ghRC_T}{U^2 + V^2} \quad (7)$$

The parameters  $s_x$  and  $s_y$  = bed slopes in the  $x$  and  $y$  directions, respectively, while  $u_*$  and  $v_*$  represent the shear velocities in the  $x$  and  $y$  directions, respectively. The shear velocities are defined as

$$u_*^2 = c_D U \sqrt{U^2 + V^2} \quad (8)$$

$$v_*^2 = c_D V \sqrt{U^2 + V^2} \quad (9)$$

where  $c_D$  = bed drag coefficient. A typical range of values presented by Parker et al. (1987) is 0.002–0.06. The smaller values are associated with relatively larger scale flows, while the larger values are associated primarily with laboratory simulations.

The volume fraction of the  $i$ th sediment present in the bed is represented by  $p_i$ , while  $E_{s_i}$  is the  $i$ th sediment entrainment coefficient. The expression, developed by Garcia and Parker (1991) and further modified by Garcia and Parker (1993), is used for closure, i.e.

$$E_{s_i} = \frac{1.3 \times 10^{-7} Z_{m_i}^5}{1 + 4.3 \times 10^{-7} Z_{m_i}^5} \quad (10)$$

where  $Z_{m_i} = \kappa \sqrt{u_*^2 + v_*^2} / v_{s_i} f(\text{R}_{p_i})$ , and  $\kappa$  is a straining parameter defined as

$$\kappa = 1 - 0.288 \sigma_{\phi} \quad (11)$$

where  $\sigma_{\phi}$  = standard deviation of the grain-size distribution based on the phi-scale,  $\phi = \log_2 D_s$ . The function  $f$  is dependent on the particle Reynolds number,  $\text{R}_{p_i} = \sqrt{g R_i D_{s_i}} D_{s_i} / \nu$ , i.e.

$$f(\text{R}_{p_i}) = \begin{cases} \text{R}_{p_i}^{0.6}, & \text{R}_{p_i} \geq 3.5 \\ 0.586 \text{R}_{p_i}^{1.23}, & 1 < \text{R}_{p_i} < 3.5 \end{cases} \quad (12)$$

where  $c_{b_i}$  = near-bed concentration of the  $i$ th sediment. The expression developed by Garcia (1994) for poorly sorted sediments is used for its estimation. This expression is

$$\frac{c_{b_i}}{C_i} = 0.40 \left( \frac{D_i}{D_{s_g}} \right)^{1.64} + 1.64 \quad (13)$$

where  $D_{s_g}$  denotes the geometric mean size of the suspended sediment mixture. Finally,  $v_{s_i}$  is the fall velocity of the  $i$ th sediment in quiescent water. An empirical relationship developed by Dietrich (1982) is used for its estimation.

Another important consideration is that turbidity currents are driven by suspended sediment, which can be gained through entrainment and lost through deposition. Therefore, a turbidity current has the ability to alter the bed over which it flows, which may substantially affect its hydrodynamics. In order to simulate this important interaction, the equations governing the hydrodynamics have been coupled to the evolution of the bed through a bed-sediment conservation equation. The bed continuity equation is needed to keep track of the amount of loose sediment on the bed. This is critical in order to limit sediment erosion in areas where loose sediment is not covering the bed. In addition, tracking the bed elevation allows for the computation of bed slopes, which are needed to solve the momentum equations.

The bed-sediment conservation equation has the form

$$(1 - \gamma) \frac{\partial z}{\partial t} = \sum_{i=1}^{n_s} v_{s_i} (c_{b_i} \cos \theta - p_i E_{s_i}) \quad (14)$$

where  $z$  and  $\gamma$  = elevation and porosity of the bed, respectively, and it has been assumed that  $\partial\gamma/\partial t \approx 0$ . Note that  $p_i$  may also change with time. In order to compute its variation, each grain size may be considered individually, i.e.

$$(1 - \gamma) \left[ p_i \frac{\partial z}{\partial t} + z \frac{\partial p_i}{\partial t} \right] = v_{s_i} (c_{b_i} \cos \theta - p_i E_{s_i}) \quad (15)$$

where it has again been assumed that  $\gamma$  is not changing rapidly with time. Substituting the expression for  $\partial z/\partial t$  from (14) into (15) yields

$$(1 - \gamma) z \frac{\partial p_i}{\partial t} = f_{s_i} - p_i f_i \quad (16)$$

where the notation

$$f_s = \sum_{i=1}^{n_s} f_{s_i} = \sum_{i=1}^{n_s} v_{s_i} (c_{b_i} \cos \theta - p_i E_{s_i}) \quad (17)$$

has been introduced.

## FINITE-VOLUME METHOD

In order to obtain a second-order accurate scheme in time, a predictor-corrector time-stepping approach is adopted to solve the governing equations. The predictor solution can be computed by solving the equations in primitive form, for simplicity and computational efficiency. The primitive equations in generalized coordinates are

$$\frac{\partial \mathbf{W}}{\partial t} + \mathbf{A}_w \frac{\partial \mathbf{W}}{\partial \xi} + \mathbf{B}_w \frac{\partial \mathbf{W}}{\partial \eta} = \mathbf{Q}_w \quad (18)$$

where  $\xi$  and  $\eta$  are in the directions of contiguous  $j$  and  $k$  indices, respectively. The index  $j$  indicates the row number of a given cell, and  $k$  indicates its column.

The array of primitive variables are  $\mathbf{W}^T = (h, U, V, C_1, \dots, C_{n_c})$ , and the matrices  $\mathbf{A}_w$  and  $\mathbf{B}_w$  are defined as

$$\mathbf{A}_w = \begin{bmatrix} U_\xi & h\xi_x & h\xi_y & 0 & \cdots & 0 \\ gRC_T\xi_x & U_\xi & 0 & \frac{1}{2}ghR_1\xi_x & \cdots & \frac{1}{2}ghR_{n_s}\xi_x \\ gRC_T\xi_y & 0 & U_\xi & \frac{1}{2}ghR_1\xi_y & \cdots & \frac{1}{2}ghR_{n_s}\xi_y \\ 0 & 0 & 0 & U_\xi & & \\ \vdots & \vdots & \vdots & & \ddots & \\ 0 & 0 & 0 & & & U_\xi \end{bmatrix} \quad (19)$$

$$\mathbf{B}_w = \begin{bmatrix} U_\eta & h\eta_x & h\eta_y & 0 & \cdots & 0 \\ gRC_T\eta_x & U_\eta & 0 & \frac{1}{2}ghR_1\eta_x & \cdots & \frac{1}{2}ghR_{n_s}\eta_x \\ gRC_T\eta_y & 0 & U_\eta & \frac{1}{2}ghR_1\eta_y & \cdots & \frac{1}{2}ghR_{n_s}\eta_y \\ 0 & 0 & 0 & U_\eta & & \\ \vdots & \vdots & \vdots & & \ddots & \\ 0 & 0 & 0 & & & U_\eta \end{bmatrix} \quad (20)$$

where  $U_\xi = U\xi_x + V\xi_y$  and  $U_\eta = U\eta_x + V\eta_y$  and the terms  $\xi_x, \xi_y, \eta_x$ , and  $\eta_y$  are the grid transformation metrics, computed by assuming a linear mapping of  $x$  and  $y$  onto  $\xi$  and  $\eta$ . Currently,  $\xi$  and  $\eta$  are assumed to vary from 0 to 1.

The primitive source terms,  $\mathbf{Q}_w$ , are defined as

$$\mathbf{Q}_w = \begin{bmatrix} E_w \sqrt{U^2 + V^2} \\ -gRC_T s_x - u_*^2/h \\ -gRC_T s_y - v_*^2/h \\ v_{s_1}(p_1 E_{s_1} - c_{b_1}/h) \\ \vdots \\ v_{s_{n_s}}(p_{n_s} E_{s_{n_s}} - c_{b_{n_s}}/h) \end{bmatrix} \quad (21)$$

An approximate solution in cell,  $j, k$  at  $t + \Delta t/2$  is

$$\mathbf{W}_{j,k}^{n+1/2} = \mathbf{W}_{j,k}^n - \frac{\Delta t}{2} (\mathbf{A}_w \overline{\Delta \mathbf{W}}_\xi + \mathbf{B}_w \overline{\Delta \mathbf{W}}_\eta - \mathbf{Q}_w)_{j,k}^n \quad (22)$$

where  $\Delta\xi = \Delta\eta = 1$  has been substituted. Note that  $\mathbf{Q}_w$  is evaluated at the cell center. However, in simulations where the bed sediment is allowed to erode, it is often necessary to neglect  $\mathbf{Q}_w$  in order to prevent numerical instability. The overbar denotes a cell average gradient of  $\mathbf{W}$  in cell  $j, k$ , i.e.

$$\overline{\Delta \mathbf{W}}_\xi = \text{avg}(\mathbf{W}_{j,k} - \mathbf{W}_{j-1,k}, \mathbf{W}_{j+1,k} - \mathbf{W}_{j,k}) = \text{avg}(a, b) \quad (23a)$$

$$\overline{\Delta \mathbf{W}}_\eta = \text{avg}(\mathbf{W}_{j,k} - \mathbf{W}_{j,k-1}, \mathbf{W}_{j,k+1} - \mathbf{W}_{j,k}) = \text{avg}(a, b) \quad (23b)$$

There are various choices for the averaging function,  $\text{avg}(\cdot)$ . However, any linear average will not preserve the monotonicity of the solution. Nonlinear averages have been specifically designed for such a purpose and have been termed flux limiters. The basic philosophy in the design of such limiters is that they preserve monotonicity of the solution by becoming first-order accurate near discontinuities, yet remain second-order accurate in regions of smooth flow. In the present model, the  $\beta$  family of averages is used and is given by

$$\overline{\Delta \mathbf{W}} = \begin{cases} \text{sign}(a) \min[\max(|a|, |b|), \beta \min(|a|, |b|)] & ab > 0 \\ 0 & ab \leq 0 \end{cases} \quad (24)$$

where  $\beta$  should be selected such that  $1 \leq \beta \leq 2$ . Note that  $\beta = 1$  yields the relatively more dissipative Minmod average, while  $\beta = 2$  yields the less dissipative Superbee average. Setting  $\overline{\Delta \mathbf{W}} = 0$  at extrema tends to flatten smooth waves, particularly as  $\beta \rightarrow 2$ . This effect can be reduced by selecting smaller values of  $\beta$ , at the expense of introducing additional numerical dissipation into the solution (Sweby 1984; Hirsch 1990). Alternatively, a higher-order spatial approximation could be implemented, which would help to distinguish between numerical extrema and physical waves. However, this would enlarge the computational stencil and reduce the efficiency of the method. Note that  $\beta = 2$  is used in all simulations.

The corrector solution is obtained from the conservative form of the governing equations. If  $\mathbf{U}$  and  $\mathbf{Q}$  are treated as average (piecewise constant) values in a region with area  $\Omega$ , while  $\mathbf{F}$  and  $\mathbf{G}$  are taken as average boundary values on  $\partial\Omega$ , then a discrete form of (1) can be obtained as

$$\Omega \frac{(\mathbf{U}^{n+1} - \mathbf{U}^n)}{\Delta t} - \mathbf{F}_{\perp 1}^{n+1/2} \Delta s_1 + \mathbf{F}_{\perp 2}^{n+1/2} \Delta s_2 + \mathbf{F}_{\perp 3}^{n+1/2} \Delta s_3 - \mathbf{F}_{\perp 4}^{n+1/2} \Delta s_4 = \mathbf{Q}^{n+1/2} \Omega \quad (25)$$

where  $\Delta t$  denotes the time increment and  $n + 1$  denotes the time level of the solution. In this study, the region has been taken to be a quadrilateral, and the indices indicate the faces of the cell while  $\Delta s$  is the cell face length. The index 1, for example, denotes the bottom cell face, while the others are numbered in a counter-clockwise manner, as illustrated in Fig. 2.

The flux  $\mathbf{F}_\perp$  is positive in the direction of increasing computational coordinates, normal to the cell boundary, and is defined as

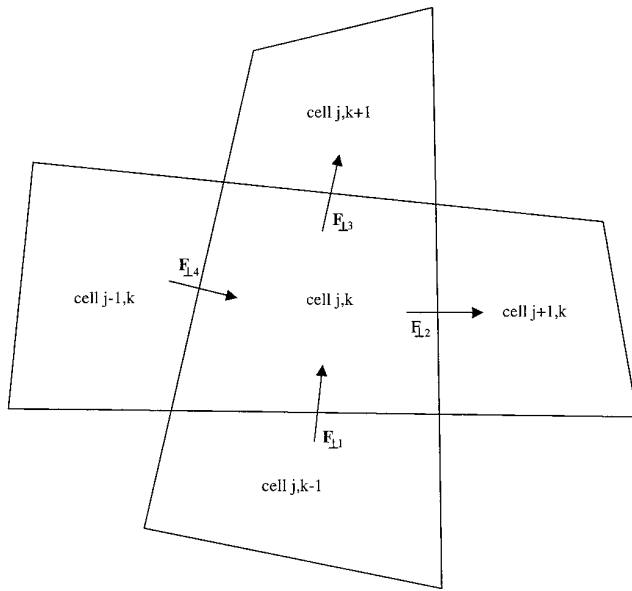


FIG. 2. Sketch of Typical Computational Cell

$$\mathbf{F}_\perp = \begin{bmatrix} hU_\perp \\ hUU_\perp + \frac{1}{2}gh^2RC_T \cos \phi \\ hVU_\perp + \frac{1}{2}gh^2RC_T \sin \phi \\ hC_1U_\perp \\ \vdots \\ hC_{n_s}U_\perp \end{bmatrix} \quad (26)$$

where  $U_\perp$  = velocity perpendicular to the cell face, and  $\phi$  = angle between the face normal and the  $x$  axis.

There are a variety of methods for computing the interfacial fluxes in (25). In the present model, a Riemann problem is solved, approximately, at each interface (Roe 1981). This method was first developed for application to the compressible Euler equations and has since been applied to the shallow water equations by several researchers. The scheme can be summarized with the following equation:

$$\mathbf{F}_{\perp I} = \frac{1}{2}(\mathbf{F}_{\perp L} + \mathbf{F}_{\perp R} - \hat{\mathbf{R}}|\hat{\mathbf{\Lambda}}|\Delta\hat{\mathbf{V}}) \quad (27)$$

where the subscript  $I$  denotes the interface between two adjacent cells, and the subscripts  $L$  and  $R$  refer to the left and right states with respect to the interface.  $\Delta$  denotes the finite difference across the cell interface.

Predicted values to the left and right of each face in a cell are first reconstructed, i.e., at the right cell face:

$$\mathbf{W}_{j+1/2,k}^{n+1/2L} = \mathbf{W}_{j,k}^{n+1/2} + \frac{1}{2}\Delta\overline{\mathbf{W}}_\xi|_{j,k}^n \quad (28a)$$

$$\mathbf{W}_{j+1/2,k}^{n+1/2R} = \mathbf{W}_{j+1,k}^{n+1/2} - \frac{1}{2}\Delta\overline{\mathbf{W}}_\xi|_{j+1,k}^n \quad (28b)$$

Similar expressions may be written for the other cell faces. This technique was first introduced by Van Leer (1979) and is known as the monotone upstream scheme for conservation laws (MUSCL). These reconstructed predictor values define a Riemann problem at each cell face, which can be used to compute  $\mathbf{F}_{\perp I}$  in (27).

The matrix  $|\hat{\mathbf{\Lambda}}|$  is diagonal and contains approximations of the absolute value of the eigenvalues of the Jacobian of  $\mathbf{F}_\perp$  at the cell interface. Specifically, the matrix is

$$|\hat{\mathbf{\Lambda}}| = \begin{bmatrix} |\hat{u}_\perp - \hat{a}| & & & & \\ & |\hat{u}_\perp| & & & \\ & & |\hat{u}_\perp + \hat{a}| & & \\ & & & |\hat{u}_\perp| & \\ & & & & \ddots \\ & & & & & |\hat{u}_\perp| \end{bmatrix} \quad (29)$$

where  $a$  denotes the celerity of a simple internal wave.

The columns of  $\hat{\mathbf{R}}$  contain the corresponding right eigenvectors, which are written as

$$\hat{\mathbf{R}} = \begin{bmatrix} 1 & 0 & 1 & 1 & \cdots & 1 \\ \hat{u} - \hat{a} \cos \phi & -\sin \phi & \hat{u} + \hat{a} \cos \phi & \hat{u} & \cdots & \hat{u} \\ \hat{v} - \hat{a} \sin \phi & \cos \phi & \hat{v} + \hat{a} \sin \phi & \hat{v} & \cdots & \hat{v} \\ \hat{c}_1 & 0 & \hat{c}_1 & -\hat{c}_T & & \\ \vdots & \vdots & \vdots & & \ddots & \\ c_{n_s} & 0 & c_{n_s} & & & -\hat{c}_T \end{bmatrix} \quad (30)$$

The characteristic variables, defined as  $\Delta\hat{\mathbf{V}} = \hat{\mathbf{\Lambda}}\Delta\mathbf{U}$ , have also been introduced, where the rows of  $\hat{\mathbf{\Lambda}}$  contain the corresponding left eigenvectors. The approximate characteristic variables can be shown to be

$$\Delta\hat{\mathbf{V}} = \begin{bmatrix} \frac{1}{2} \left( \Delta h - \frac{\hat{h}\Delta u_\perp}{\hat{a}} + \frac{\hat{h}\Delta c_T}{2c_T} \right) \\ \hat{h}\Delta u_\parallel \\ \frac{1}{2} \left( \Delta h + \frac{\hat{h}\Delta u_\perp}{\hat{a}} + \frac{\hat{h}\Delta c_T}{2c_T} \right) \\ \frac{\hat{h}}{\hat{c}_T} \left( \frac{\hat{c}_1\Delta c_T}{2\hat{c}_T} - \Delta c_1 \right) \\ \vdots \\ \frac{\hat{h}}{\hat{c}_T} \left( \frac{\hat{c}_{n_s}\Delta c_T}{2\hat{c}_T} - \Delta c_{n_s} \right) \end{bmatrix} \quad (31)$$

where  $u_\parallel$  = velocity parallel to the cell face.

The quantities denoted with a hat are known as Roe averages and are computed as follows:

$$\hat{h} = \sqrt{h_L h_R} \quad (32a)$$

$$\hat{u} = \frac{\sqrt{h_L}U_L + \sqrt{h_R}U_R}{\sqrt{h_L} + \sqrt{h_R}} \quad (32b)$$

$$\hat{a} = \sqrt{\frac{gR}{2}(h_L C_L + h_R C_R)} \quad (32c)$$

The averages,  $\hat{v}$  and  $\hat{c}_i$ , are computed in a manner analogous to  $\hat{u}$ .

One problem with the above scheme is that it treats a finite width depression wave as a wave with infinitesimal width traveling with an average speed  $\hat{\lambda} = \hat{u}_\perp \pm \hat{a}$ , which are called the wave eigenvalues. This can cause problems when the interface between two cells contains a critical flow point. In such a case, one of the wave eigenvalues will be very close to, or perhaps equal to, zero, and no flux contribution is computed for this wave. A result of this is that a shock wave is computed within the depression wave, which either decays too slowly or not at all.

One way to correct this is to introduce a local depression wave whenever  $\lambda_L \leq 0 \leq \lambda_R$  at a cell interface (Hirsch 1990).

This can be accomplished by replacing  $|\hat{\lambda}|$  with the following relation:

$$|\hat{\lambda}|^* = \frac{\hat{\lambda}^2}{\Delta\lambda} + \frac{\Delta\lambda}{4} \quad (33)$$

where  $\Delta\lambda = 4(\lambda_R - \lambda_L)$  yields the appropriate amount of dissipation when marching to a steady-state, as shown by Van Leer et al. (1989). This relation should be used whenever a critical point occurs at an interface, i.e., when  $-\Delta\lambda/2 < |\hat{\lambda}| < \Delta\lambda/2$ , in place of  $|\hat{\lambda}|$  for the wave eigenvalues only. The other eigenvalues,  $\lambda = \hat{u}_\perp$ , should never be modified.

## BOUNDARY CONDITIONS

Typical boundary conditions used in this study are solid-wall, outflow, and specified inflow. The implementation of boundary conditions is accomplished through the use of a ghost cell at the boundary, but one outside the domain of interest. By placing the appropriate quantities in the ghost cell, the flux at the boundary can then be solved for in the manner previously described. This is not only convenient but it also automatically incorporates the characteristic theory embedded in Roe's Riemann solver, allowing for a physically correct treatment at the boundary.

For example, for a supercritical inflow boundary, the specified flow thickness, velocity, and sediment concentration are placed in the ghost cell and  $\Delta\bar{\mathbf{W}}_\xi = \Delta\bar{\mathbf{W}}_\eta = 0$  is enforced. The choice of specifying primitive variables is made for convenience. Conservative or characteristic variables could likewise be specified. If the inflow is subcritical, only two independent quantities may be specified. The remaining quantity is extrapolated from the flow domain.

At a supercritical outflow boundary ( $U > a$ ), the primitive variables are linearly extrapolated from the domain while the gradients are zero-order extrapolated. This maintains the overall accuracy of the model (Hirsch 1990). At a subcritical outflow boundary ( $U < a$ ), the primitive variables are zero-order extrapolated from the domain and the gradients are set to zero, maintaining the stability of the solution.

At a solid wall, the reflections of the velocities perpendicular and parallel to the boundary wall are placed in the ghost cell such that the perpendicular velocity at the wall is zero while the parallel velocity remains unchanged. These criteria lead to the following conditions:

$$h_g = h_{in} \quad (34a)$$

$$U_g = U_{in}(\sin^2\phi - \cos^2\phi) - 2V_{in} \sin\phi \cos\phi \quad (34b)$$

$$V_g = -2U_{in} \sin\phi \cos\phi + V_{in}(\cos^2\phi - \sin^2\phi) \quad (34c)$$

$$C_g = C_{in} \quad (34d)$$

where the subscript  $g$  refers to the ghost cell, and the subscript  $in$  refers to the cell adjacent to the boundary but inside the domain of interest. Assuming that the boundary is perpendicular to the  $\xi$  direction, then the gradients are set as follows:

$$\Delta\bar{h}_\xi|_g = -\Delta\bar{h}_\xi|_{in} \quad (35a)$$

$$\Delta\bar{U}_\xi|_g = \Delta\bar{U}_\xi|_{in}(\cos^2\phi - \sin^2\phi) + 2\Delta\bar{V}_\xi|_{in} \sin\phi \cos\phi \quad (35b)$$

$$\Delta\bar{V}_\xi|_g = 2\Delta\bar{U}_\xi|_{in} \sin\phi \cos\phi + \Delta\bar{V}_\xi|_{in}(\sin^2\phi - \cos^2\phi) \quad (35c)$$

$$\Delta\bar{C}_\xi|_g = -\Delta\bar{C}_\xi|_{in} \quad (35d)$$

while the gradients in the  $\eta$  direction are set to zero.

## "DRY" BED COMPUTATIONS

In order to simulate episodic, deep sea turbidity currents, the model must be capable of solving problems in which  $h \rightarrow$

0. At such locations, the bed is "dry" from a numerical viewpoint although it is actually covered with ambient fluid. Such a possibility poses little additional difficulty for the proposed method. At an interface between a wet and a dry cell, a Riemann problem exists and therefore the flux can be computed with the aid of Roe's approximate Riemann solver. Bradford (1996) showed that the computed fluxes at a wet-dry interface are equivalent to the ones that would be obtained from an extrapolation from the center of the wet cell to the interface. Extrapolation from the interior of the flow to the frontal boundary is mathematically appropriate since the flow there is supercritical when considering a fixed-volume release of turbid flow (Huppert and Simpson 1980). The fluxes are set to zero at faces with no adjacent wet cells.

An extra precaution must be taken to insure that the front

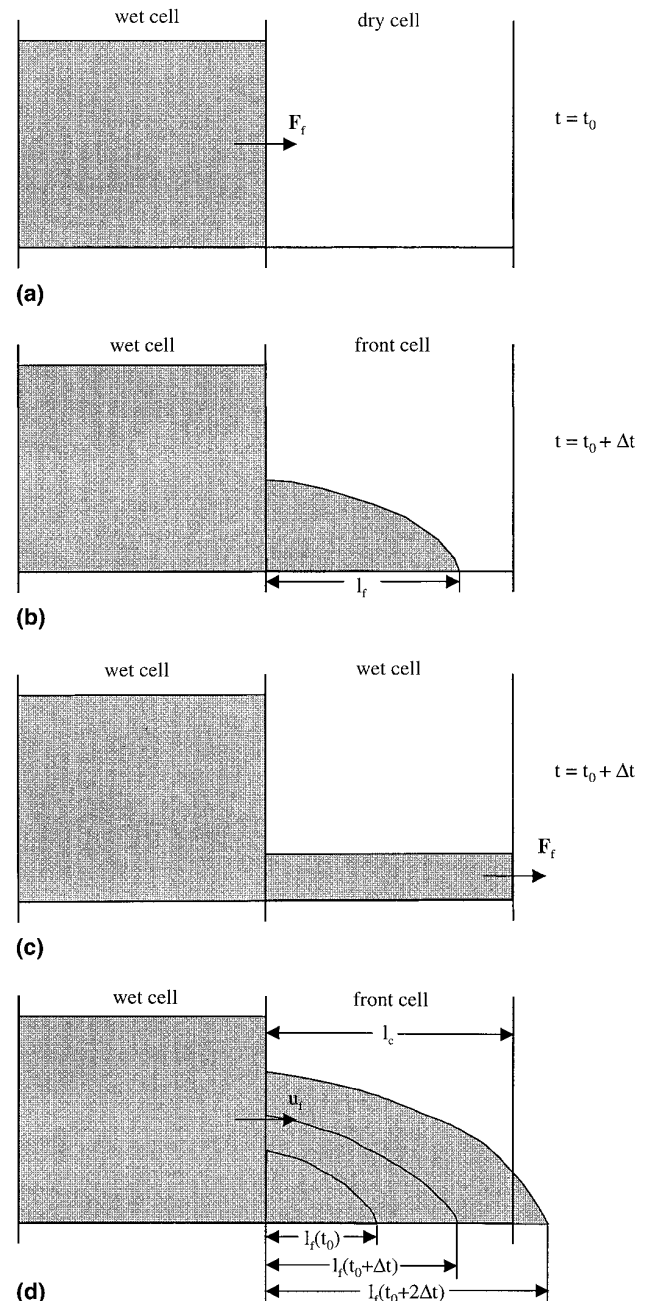


FIG. 3. Conceptual Sketch (a) of Wet-Dry Interface; (b) of Actual Wetting Front; (c) Numerical Treatment of Wetting Front; (d) Sketch of Proposed Front Tracking Scheme

does not propagate at an artificially high speed. Consider a wet cell next to a dry cell, as shown in Fig. 3(a). Frontal fluxes,  $F_f$ , are computed at the interface, and physically the front will travel a distance  $l_f$  into the adjacent dry cell, as shown in Fig. 3(b). However, since the depth is represented by a cell-centered average value, the interface between the newly wetted cell and the next neighboring dry cell becomes wetted, and fluxes at the next time step will be computed there as shown in Fig. 3(c). This results in the artificial spreading of the front. To avoid this problem, the front is tracked by keeping account of the incremental advance length  $l_f$ , which is estimated as

$$l_f(t_0 + \Delta t) = l_f(t_0) + u_f \Delta t \quad (36)$$

where  $u_f$  denotes the propagation speed of the front and  $t_0$  is some arbitrary time level. If  $l_f$  is less than the cell dimension in the direction of propagation,  $l_c$ , then the downstream fluxes in the frontal cell are set to zero, as shown in Fig. 3(d). When  $l_f > l_c$ , the downstream fluxes are computed in the usual manner.

There are various alternatives for determining  $u_f$ . Bonnetaze et al. (1995) used the empirically determined expression

$$u_f = F_f \sqrt{g R h_f C_{Tf}} \quad (37)$$

as a frontal boundary condition for the velocity. Note that  $F_f$  is an experimentally determined value of the internal Froude number at the front while  $h_f$  and  $C_{Tf}$  are the front depth and total sediment concentration, respectively. For a sudden release of a fixed volume of turbid fluid in a flat channel, Huppert and Simpson (1980) measured  $F_f = 1.19$ . However, this method is unsatisfactory because  $F_f$  is influenced by the method of flow initiation, i.e., fixed flux or fixed-volume release. Also, there is no general expression for 2D flow over arbitrary bathymetry. Therefore, in the present model  $u_f$  is determined directly from the computed values of  $U$  and  $V$  in the newly wetted cell. This is a more general approach that allows for the inclusion of arbitrary bathymetry and ambient fluid entrainment through  $Q$ .

There is also the possibility that the wetting front would propagate further than one cell per time step. However, the explicit time-stepping scheme of the present model requires that  $\Delta t$  be selected so that it limits the travel distance to one cell length in order to maintain the stability of the solution. Therefore, this case is not a concern. There is one exception, however, corresponding to the case of an ideal turbidity current with  $Q = 0$ . Bradford et al. (1997) showed that the wetting front due to a fixed-volume release travels with a speed twice the maximum eigenvalue of the system and therefore, in this instance, the model always underpredicts the propagation speed. This problem may be overcome by modifying Roe's method to specifically account for this case. Fraccarollo and Toro (1995) have recently done this for the shallow water equations. However, since ideal turbidity currents are not of interest in this study, such modifications were not performed here.

The proposed approach is simple, robust, and requires no empirical parameters, contrary to moving grid techniques, which are difficult to implement and require additional computational effort to regenerate the numerical grid at each time-step. In addition, grid moving methods are subject to severe cell deformation and node crossing, particularly when modeling highly transient events over variable bathymetry. Sloff (1997) assumed that the entire domain was covered with a thin layer of fluid and treated the front as a shock wave. However, this is not a satisfactory approach when a sharp interface between truly wet and dry regions of the domain is desired, so it is not considered in the present model. However, there is an additional complication with the proposed technique. It must be decided how small  $h$  should be before the corresponding

cell is considered dry. This is needed in order to prevent a division by zero when computing velocity components and sediment concentrations from the volume fluxes  $hU$ ,  $hV$ , and  $hC$ , as well as evaluating  $Q_w$ . A tolerance,  $\epsilon_h$ , is utilized for differentiating between wet and dry cells; for example, when  $h < \epsilon_h$ ,  $U$ ,  $V$ , and  $C$  are kept at their previous time values and  $Q_w = 0$  is enforced. The value  $\epsilon_h = 1 \times 10^{-5}$  m is utilized in all the following simulations, which is large enough to prevent numerical instability in the simulations but small enough not to artificially hinder the progression of the wetting front.

## SOLUTION OF BED CONTINUITY EQUATION

The bed continuity equation can be solved after the flow properties have been obtained. If  $z$  is assumed to be a cell average value of the bed elevation, then (14) can be written as an ordinary differential equation within a cell. In order to maintain second-order accuracy, Heun's predictor-corrector method may be utilized to integrate the equation. Since the net sediment flux is independent of  $z$ , Heun's method reduces to the well known trapezoidal rule of integration

$$z_{j,k}^{n+1} = z_{j,k}^n + \frac{\Delta t}{2(1 - \gamma)} (f_s^{n+1} + f_s^n)_{j,k} \quad (38)$$

where  $z_{j,k}$  = cell average bed elevation and  $f_s$  is defined in (17). In order to avoid computing an iterative solution, it is assumed that  $p_i^{n+1} \approx p_i^n$ . The resulting bed elevations are then used to compute the bed slope terms needed to solve the momentum equations at the next time level. This provides the vital link between the turbidity current and its surroundings, which is needed to realistically simulate the mechanics of the current and the corresponding evolution of the bed.

The new volume fraction of each sediment in the cell is computed in an analogous manner. However, because the sediment fluxes depend on  $p_i$ , Heun's method does not reduce to the trapezoidal rule. Therefore, a predictor is computed in each cell as

$$\tilde{p}_i = p_i^n + \frac{\Delta t}{(1 - \gamma)} \left( \frac{f_{s_i} - p_i f_s}{z} \right)_{j,k}^n \quad (39)$$

The corrector in each cell is computed as

$$p_i^{n+1} = p_i^n + \frac{\Delta t}{2(1 - \gamma)} \left[ \left( \frac{f_{s_i} - p_i f_s}{z} \right)^n + \left( \frac{\tilde{f}_{s_i} - \tilde{p}_i \tilde{f}_s}{z} \right)^{n+1} \right]_{j,k} \quad (40)$$

where  $\tilde{f}_{s_i}$  and  $\tilde{f}_s$  are the sediment fluxes evaluated with  $\tilde{p}_i$ .

## MODEL VERIFICATION

Comparisons of numerical predictions with the experimental data measured by Bonnetaze et al. (1995) are presented for model verification. The experiments consisted of a fixed volume release of turbid fluid in an axisymmetric flume illustrated in Fig. 4. The smaller lock length corresponds to experiments that utilized a sediment with  $D_s = 37 \mu\text{m}$ , while the longer lock length corresponds to experiments performed with  $D_s = 23 \mu\text{m}$ . Both sediments were silicon carbide particles with  $R = 2.217$  and three different initial sediment concentrations were utilized (0.0193, 0.00966, and 0.00506). In all cases, the initial height of turbid fluid in the lock was equal to 0.14 m.

The numerical discretization consisted of 5 cells in the cross-channel direction and 280 cells along the length of the channel. Values of  $c_b = 0.01$ , 0.02, and 0.03 were used to illustrate model sensitivity to bed drag. These values constitute a plausible range for small scale turbidity currents as previously discussed. In addition,  $c_b = C$  was utilized instead of (13), the derivation of which assumes that the turbidity current is fully developed and that vertical gradients of the sediment

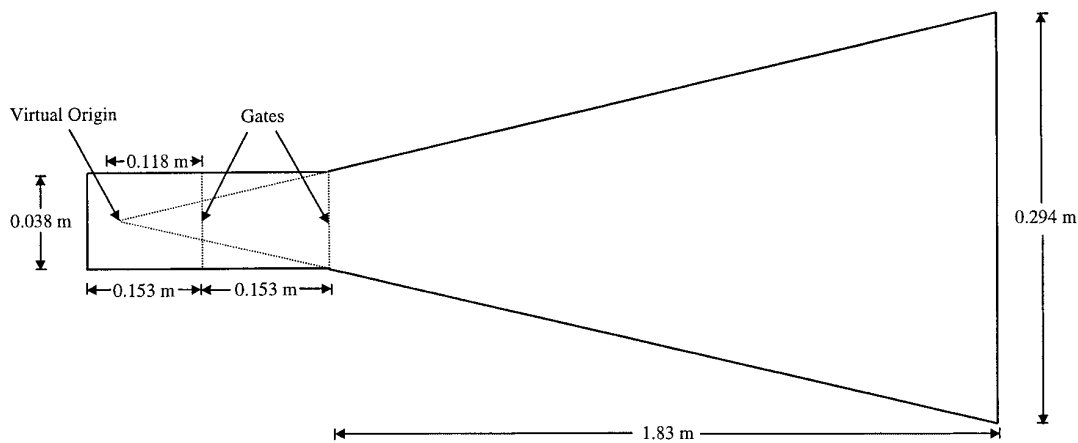


FIG. 4. Plan View Sketch of Axisymmetric Laboratory Flume (Not to Scale)

concentration are established. For this problem however, the turbid fluid was well mixed prior to release. Much of the sediment settled out soon after the gate was removed, before the flow could fully develop. Thus, specifying  $c_b = C$  is appropriate.

Fig. 5(a) shows a comparison of the predicted and measured frontal positions as a function of time for the  $D_s = 23 \mu\text{m}$  case. The frontal position was measured from the virtual origin shown in Fig. 4. In this figure, results with  $c_D = 0.02$  are presented. Increasing the drag coefficient led to modest reductions in the propagation speed of the front, while reducing  $c_D$  slightly increased the speed. In Fig. 5(a) it is seen that the model captures the correct trend of increasing frontal speed with increasing initial sediment concentration. However, the model consistently overpredicts the propagation speed as compared to the measured data. This is more likely due to the fact that the experiments were performed in shallow water, which invalidates the single layer model formulation, and not to any shortcoming of the front tracking scheme. When a turbidity current intrudes shallow water, an opposing current is generated in the ambient fluid, which acts to increase the drag on the turbidity current and reduce its forward momentum. In spite of this, however, the model was able to accurately predict sedimentation as shown below. Thus this indicates that the speed of the front of the turbidity current has a minimal impact on resulting bed morphology. Similar results were obtained for the  $D_s = 37 \mu\text{m}$  case as shown in Fig. 5(b).

Figs. 6(a–c) show comparisons of the numerical and experimental bed deposit density as a function of radial distance from the virtual origin for  $D_s = 23 \mu\text{m}$ . Bed deposit density is defined as the mass of deposited sediment per unit area of the channel bed and the plotted values are averages over the bed for a given  $r$ . From the figures it is seen that the agreement between observed and predicted values is very good, particularly away from the gate. Larger values of  $c_D$  yielded better predictions of distal settling, but  $c_D = 0.02$  seemed to best match the measurements. Figs. 7(a–c) show comparisons with  $D_s = 37 \mu\text{m}$  and again, model predictions agree very well with the measurements.

The previous experiments involved turbidity currents consisting of uniform sediment. Additional tests were performed to examine the model's ability to simulate poorly sorted sediments. Model predictions for bed deposition were compared with experimental data gathered by Middleton and Neal (1989). The experiments again consist of the sudden release of a fixed volume turbidity current into a flume. In this case, however, the flume is rectangular and is 6 m long, 0.15 m wide, and 0.5 m deep. The gate is located 0.29 m from the upstream end. Three sediments, consisting of glass beads, were

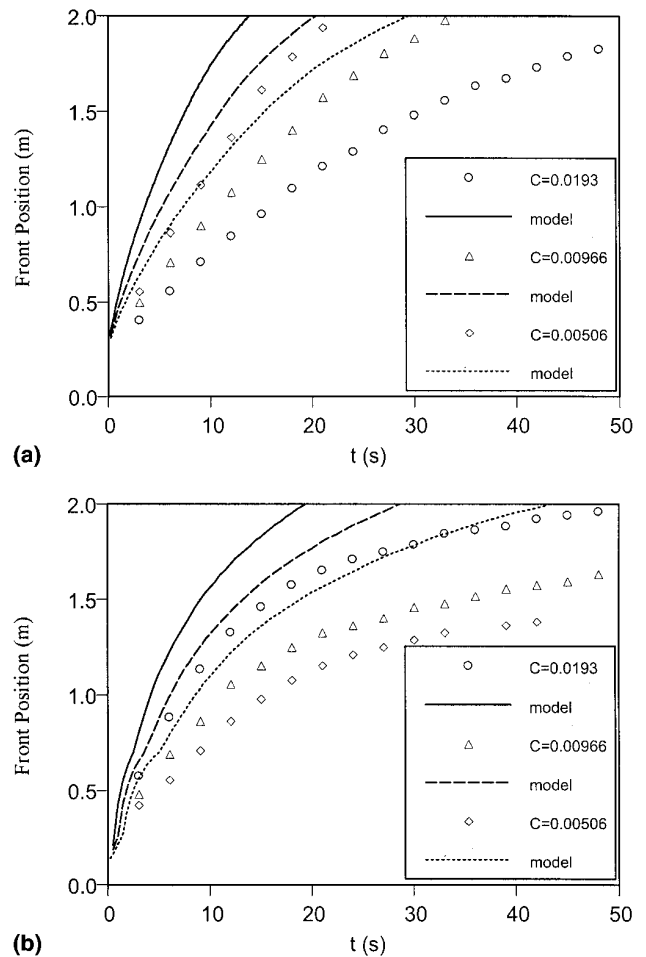
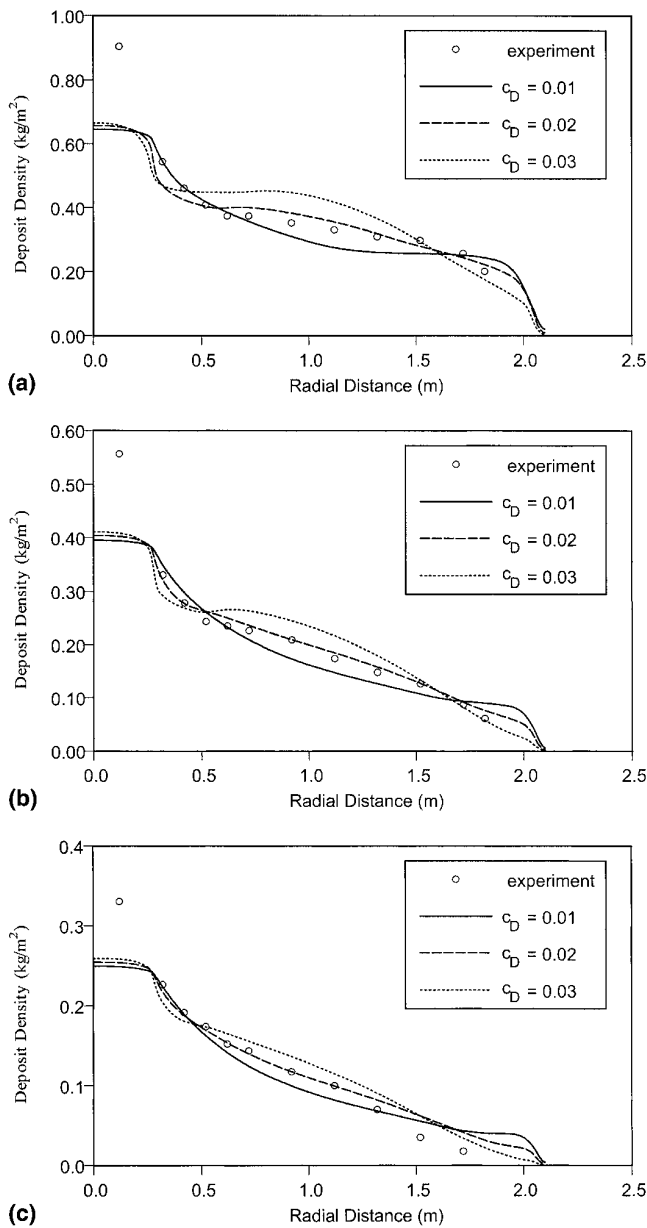


FIG. 5. Comparison of Numerical (lines) and Experimental (symbols) Frontal Position for Fixed-Volume Releases of Turbid Fluid with (a)  $D_s = 23 \mu\text{m}$ ; (b)  $D_s = 37 \mu\text{m}$

used with  $D_s = 85 \mu\text{m}$   $R = 1.4$ ,  $D_s = 156 \mu\text{m}$   $R = 1.47$ , and  $D_s = 258 \mu\text{m}$   $R = 1.45$ . Numerical results are presented for a mixture of equal volumes of the smallest and largest sediments. The initial fluid height was 0.2 m, while two different initial sediment concentrations, equal to 0.2 and 0.4, were used. These concentrations are very high, and therefore beyond the valid range of the model's capability. However, much of the sediment settles immediately, thus reducing the flow



**FIG. 6. Comparison of Predicted (lines) and Experimental (symbols) Bed Deposit Density as Function of Radial Distance from Virtual Origin,  $r$  for Fixed-Volume Releases of Turbid Fluid with  $D_s = 23 \mu\text{m}$  and (a) Initial  $C = 0.0193$ ; (b) Initial  $C = 0.00966$ ; (c) Initial  $C = 0.00506$**

sediment concentration to a level which is closer to the range of validity of the model.

There is an additional complication associated with these data. The experimental results were presented as measurements of the thickness of the bed taken prior to the drainage of the tank. In this case, an additional parameter must be specified, which is the porosity of the bed. The measured bed profiles were integrated in order to compute the volumes of the beds. These values were then used along with the original sediment volumes to compute the bed porosities. For the sediment mixture,  $\gamma = 0.20$  was estimated. This value is somewhat low, but it is used in the numerical simulations to compute the bed elevation.

Fig. 8(a) shows the resulting bed profile for an initial  $C = 0.2$ , using the same three values of  $c_D$ . Once again the model matches the experimental data beyond the gate reasonably

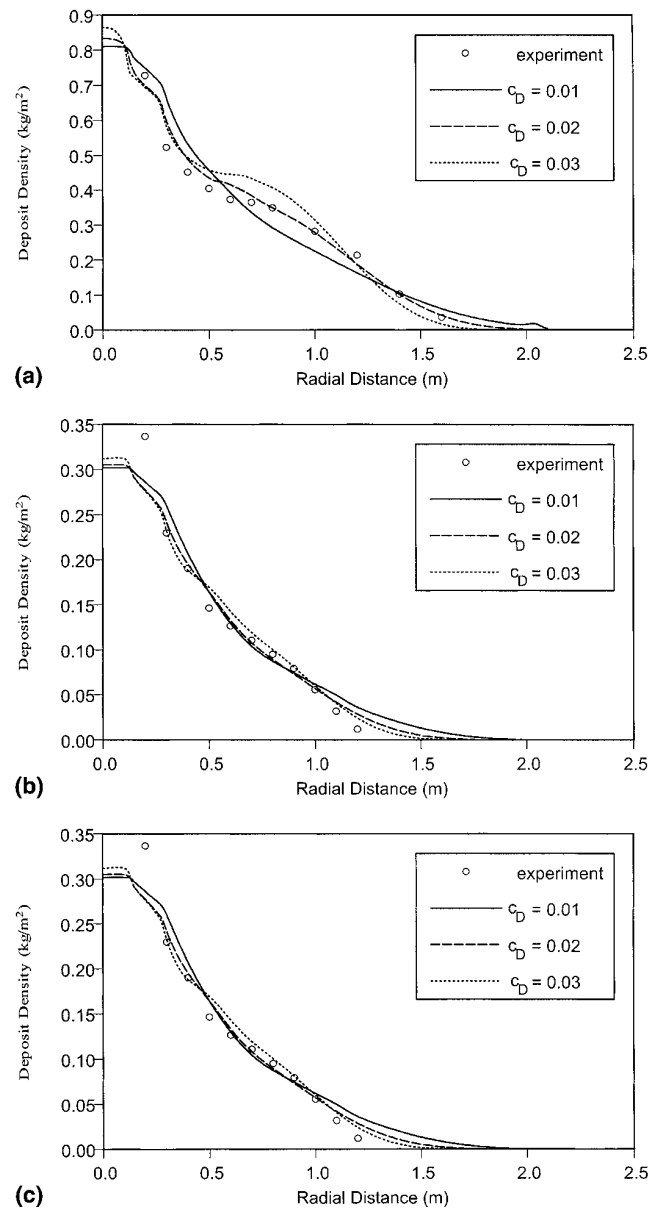


**FIG. 7. Comparison of Predicted (lines) and Experimental (symbols) Bed Deposit Density as Function of Radial Distance from Virtual Origin,  $r$  for Fixed-Volume Releases of Turbid Fluid with  $D_s = 37 \mu\text{m}$  and (a) Initial  $C = 0.0193$ ; (b) Initial  $C = 0.00966$ ; (c) Initial  $C = 0.00506$**

well, particularly for the two larger values of  $c_D$ . While the agreement between predicted and experimental deposit thickness is acceptable, the model seems to slightly overpredict the extent of distal settling. This may be attributable to the fact that the flow is actually a two-layer flow, while the model assumes that it is a single-layer flow. As previously discussed, a single-layer flow has less drag acting on it and therefore will travel faster, thus carrying sediment further before deposition occurs.

Fig. 8(b) shows the resulting bed profile for an initial  $C = 0.4$ . The model predictions do not agree with the measurements as well as in the previous case, which is probably due to the very high initial sediment concentration in this case. Initially, settling may be hindered due to the matrix strength of the flow provided by grain interactions. This would allow more sediment to be transported further downstream of the gate. Such a scenario is not accounted for by the model and



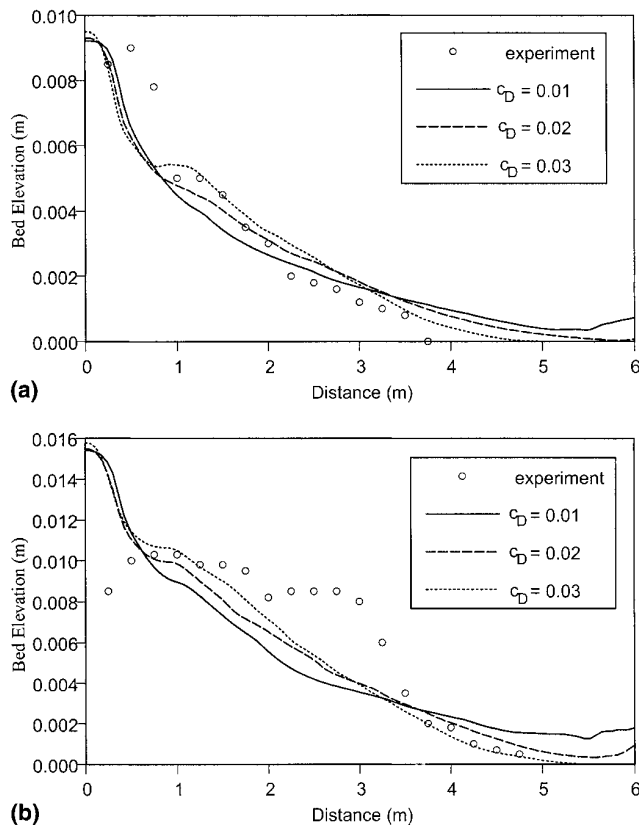


**FIG. 8. Comparison of Predicted (lines) and Experimental (symbols) Bed Elevation as Function of Distance along Channel Axis for Sediment Mixture with (a) Initial  $C = 0.2$ ; (b) Initial  $C = 0.4$**

therefore deposition is overpredicted behind the gate and less deposition is predicted downstream of the gate.

## CONCLUSIONS

The presented model is quite general and can simulate 2D, time-dependent turbidity currents driven by nonuniform sediment. Sediment entrainment and deposition are explicitly accounted for, which allows for the simulation of turbidite growth and evolution. It has the ability to realistically simulate the flow hydrodynamics as well as the resulting sedimentation, as illustrated by the comparisons of model predictions with experimental data for flows driven by uniform and nonuniform sediment.

The mathematical foundation of the model consists of the fluid, momentum, and sediment conservation laws for the hydrodynamics, and a bed sediment conservation equation for the bed dynamics. The most advanced empirical relations have been used for model closure and treatment of sediment transport. However, the use of sophisticated empirical relations is irrelevant if the conservation laws are inaccurately solved. Error introduced by some numerical techniques can corrupt and dominate the solution. Therefore, careful consideration and selection of the numerics is crucial. The finite volume method was selected because it is an ideal technique for solving hyperbolic, time-dependent equations such as the conservation laws. The method accurately captures waves, preserves the monotonicity of the solution, and is computationally efficient. This method's accuracy and robustness have been thoroughly demonstrated by comparing model predictions with independent laboratory data, which was, in most cases, very satisfactory.

However, the treatment of the wetting front requires further investigation. The proposed method is attractive since it is easy

to implement, completely general for all types of flows, and requires no empirical tuning parameters. However, the fluid entrainment function employed by the model was developed for steady flows and may not be applicable to the wetting front. This is further discussed in part two of this paper. Additional data for single layer currents are needed to make a complete assessment of this approach.

The presented model is a simplified representation of the flow and sedimentary processes which occur in subaqueous turbidity currents. The model represents an initial effort to quantify the effects of basin morphology and sediment properties on the mechanics of turbidity currents and of the characteristics of the resulting deposits. Many numerical experiments involving the simulation of deep-sea turbidity currents could be performed in order to better understand their behavior and the impact on sea bed morphology, the results of some of which are presented in the companion paper.

## ACKNOWLEDGMENTS

The finite-volume model in this paper was inspired by similar developments in compressible gas dynamics carried out at the Aerospace Engineering Department of the University of Michigan. The authors wish to express their gratitude to Philip Roe and Bram van Leer for numerous suggestions during the development stages of the model.

## APPENDIX I. REFERENCES

- Bonnecaze, R. T., Hallworth, M. A., Huppert, H. E., and Lister, J. R. (1995). "Axisymmetric particle-driven gravity currents." *J. Fluid Mech.*, 294, 93–121.
- Bonnecaze, R. T., Huppert, H. E., and Lister, J. R. (1993). "Particle-driven gravity currents." *J. Fluid Mech.*, 250, 339–369.
- Bradford, S. F. (1996). "Numerical simulation of a turbidity current hydrodynamics and sedimentation," PhD dissertation, University of Michigan, Ann Arbor, Mich.
- Bradford, S. F., Katopodes, N. D., and Parker, G. (1997). "Characteristic analysis of turbid underflows." *J. Hydr. Engrg.*, ASCE, 123(5), 420–431.
- Dengler, A. T., and Wilde, P. (1987). "Turbidity currents on steep slopes: Application of an avalanche-type numeric model for ocean thermal energy conversion design." *Ocean Engrg.*, 14, 409–433.
- Dietrich, W. E. (1982). "Settling velocity of natural particles." *Water Resour. Res.*, 18, 1615–1626.
- Flood, R. D., and Damuth, J. E. (1987). "Quantitative characteristics of sinuous distributary channels of the Amazon deep-sea fan." *Geolog. Soc. of Am. Bull.*, 98, 728–738.
- Fraccarollo, L., and Toro, E. F. (1995). "Experimental and numerical assessment of the shallow water model for two-dimensional dam-break type problems." *J. Hydr. Res.*, ASCE, 33, 843–864.
- Garcia, M. H. (1994). "Depositional turbidity currents laden with poorly sorted sediment." *J. Hydr. Engrg.*, ASCE, 120(11), 1240–1263.
- Garcia, M., and Parker, G. (1991). "Entrainment of bed sediment into suspension." *J. Hydr. Engrg.*, ASCE, 117(4), 414–435.
- Garcia, M., and Parker, G. (1993). "Experiments on the entrainment of sediment into suspension by a dense bottom current." *J. Geophys. Res.*, 98(C3), 4793–4807.
- Hay, A. E. (1987). "Turbidity currents and submarine channel formation in Rupert Inlet, British Columbia 1. Surge observations." *J. Geophys. Res.*, 92, 2875–2881.
- Heezen, B. C., and Ewing, M. C. (1952). "Turbidity currents and submarine slumps, and the 1929 Grand Banks earthquake." *Am. J. Sci.*, 250, 849–873.
- Hirsch, C. (1990). *Numerical computation of internal and external flows*. Wiley, New York.
- Hiscott, R. N. (1984). "Loss capacity, not competence, as the fundamental process governing deposition from turbidity currents." *J. Sedimentary Res.*, A64, 209–214.
- Huppert, H. E., and Simpson, J. E. (1980). "The slumping of gravity currents." *J. Fluid Mech.*, 99, 785–799.
- Imran, J., Parker, G., and Katopodes, N. (1998). "A numerical model of channel inception on submarine fans." *J. Geophys. Res.*, 103(C1), 1219–1238.
- Inman, D. L., Nordstrom, C. E., and Flick, R. E. (1976). "Currents in submarine canyons: An air-sea-land interaction." *Annu. Rev. of Fluid Mech.*, 8, 275–310.
- Komar, P. D. (1977). "Computer simulation of turbidity current flow and

- the study of deep-sea channels and fan sedimentation." *The sea*, Wiley, New York.
- Middleton, G. V. (1966). "Experiments on density and turbidity currents I. Motion of the head." *Can. J. Earth Sci.*, 3, 523–546.
- Middleton, G. V., and Neal, W. J. (1989). "Experiments on the thickness of beds deposited by turbidity currents." *J. Sedimentary Petrology*, 59, 297–307.
- Normark, W. R. (1989). "Observed parameters for turbidity-current flows in channels, Reserve Fan, Lake Superior." *J. Sedimentary Petrology*, 59, 423–431.
- Parker, G. (1982). "Conditions for the ignition of catastrophically erosive turbidity currents." *Marine Geol.*, 46, 307–327.
- Parker, G., Fukushima, Y., and Pantin, H. M. (1986). "Self-accelerating turbidity currents." *J. Fluid Mech.*, 171, 145–181.
- Parker, G., Garcia, M., Fukushima, Y., and Yu, W. (1987). "Experiments on turbidity currents over an erodible bed." *J. Hydr. Res.*, 25(1), 123–147.
- Reynolds, S. (1987). "A recent turbidity current event, Hueneme Fan, California: Reconstruction of flow properties." *Sedimentology*, 34, 129–137.
- Roe, P. L. (1981). "Approximate Riemann solvers, parameter vectors, and difference schemes." *J. Computat. Phys.*, 43, 357–372.
- Sloff, C. J. (1997). "Sedimentation in Reservoirs," PhD thesis, Delft University of Technology, Delft, The Netherlands.
- Stow, D. A. V., Howell, D. G., and Nelson, C. H. (1985). "Sedimentary, tectonic, and sea-level controls." *Submarine fans and related turbidite systems*, Springer, New York.
- Sweby, P. K. (1984). "High resolution schemes using flux limiters for hyperbolic conservation laws." *SIAM J.*, 21, 995–1011.
- Van Leer, B. (1979). "Towards the ultimate conservative difference scheme. V. A second order sequel to Godunov's method." *J. Computat. Phys.*, 32, 101–136.
- Van Leer, B., Lee, W. T., and Powell, K. G. (1989). "Sonic point capturing." *Proc., AIAA 9th Computat. Fluid Dyn. Conf.*, Buffalo, N.Y., American Institute of Aeronautics and Astronautics, Reston, Va.
- Wilde, P., Normark, W. R., Chase, T. E., and Gutmacher, C. E. (1985). "Potential petroleum reservoirs on deep-sea fans off central California." *Submarine fans and related turbidite systems*, Springer, New York.

## APPENDIX II. NOTATION

The following symbols are used in this paper:

- $\mathbf{A}_w$  = primitive Jacobian of  $\mathbf{F}$ ;  
 $a$  = celerity of simple internal wave;  
 $\hat{a}$  = Roe average of  $a$ ;  
 $\mathbf{B}_w$  = primitive Jacobian of  $\mathbf{G}$ ;  
 $C$  = vertically averaged volume concentration of sediment;

- $\hat{C}$  = Roe average of  $C$ ;  
 $c_b$  = near bed-sediment concentration;  
 $c_D$  = bed drag coefficient;  
 $E_s$  = sediment entrainment coefficient;  
 $E_w$  = ambient fluid entrainment coefficient;  
 $\mathbf{F}$  = vector of fluxes in  $x$  direction;  
 $\mathbf{F}'$  = vector of fluxes perpendicular to cell face;  
 $F_f$  = internal Froude number of wetting front;  
 $f_s$  = net sediment flux from current;  
 $\mathbf{G}$  = vector of fluxes in  $y$  direction;  
 $g$  = acceleration due to gravity;  
 $h$  = flow thickness;  
 $\hat{h}$  = Roe-averaged flow thickness;  
 $\mathbf{L}$  = matrix of left eigenvalues for 2D equations;  
 $l_c$  = cell length in wetting front propagation direction;  
 $l_f$  = propagation length of wetting front;  
 $n_{\text{sed}}$  = total number of sediments considered;  
 $p$  = volume fraction of sediment;  
 $\mathbf{Q}$  = vector of conservative source terms;  
 $R$  = ratio of density excess to density of ambient fluid;  
 $\mathbf{R}$  = matrix of right eigenvectors of  $\mathbf{A}_w$ ;  
 $Ri$  = Richardson number;  
 $t$  = temporal coordinate;  
 $U$  = vertically averaged velocity in  $x$  direction;  
 $\mathbf{U}$  = vector of conservative variables;  
 $U_\perp$  = vertically averaged velocity perpendicular to cell face;  
 $u_f$  = propagation speed of wetting front;  
 $\hat{U}$  = Roe average of  $U$ ;  
 $V$  = vertically averaged velocity in  $y$  direction;  
 $\mathbf{V}$  = vector of characteristic variables;  
 $\hat{V}$  = Roe average of  $V$ ;  
 $v_s$  = sediment fall velocity in quiescent fluid;  
 $\mathbf{W}$  = vector of primitive variables;  
 $x$  = spatial coordinate;  
 $y$  = spatial coordinate;  
 $z$  = bed elevation;  
 $\gamma$  = bed porosity;  
 $\Delta$  = jump in flow property across discontinuity;  
 $\epsilon_h$  = depth tolerance;  
 $\mathbf{\Lambda}$  = diagonal matrix of eigenvalues of  $\mathbf{A}$ ;  
 $\lambda_i$  = individual eigenvalues of  $\mathbf{A}$ ;  
 $\rho$  = ambient fluid density;  
 $\rho_s$  = sediment density;  
 $\sigma_\phi$  = standard deviation of sediment distribution;  
 $\phi$  = angle between  $x$  axis and cell face normal vector; and  
 $\Omega$  = area of computational cell.